20. OFF-AXIS ELECTRON HOLOGRAPHY

MARTHA R. McCARTNEY, RAFAL E. DUNIN-BORKOWSKI AND DAVID J. SMITH

1. ELECTRON HOLOGRAPHY AND NANOTECHNOLOGY

Nanoscale electromagnetic fields are essential for the function of many nanostructured materials and devices. Important examples include elemental and compound semiconductor p–n junctions and non-volatile magnetic storage media. Theory and modeling can be used to estimate field strengths, but direct measurements are preferable for materials that have smaller dimensions, especially to understand and control the effects of local inhomogeneities on macroscopic properties. Off-axis electron holography is an ideal technique for tackling such problems.

There are many possible imaging modes in the transmission electron microscope (TEM). Most of these suffer from the drawback that the final electron micrograph is a spatial distribution of intensity so that information about the phase shift of the electron that has passed through the sample is lost. The technique of electron holography, first proposed by Gabor [1], overcomes this limitation, and allows the electron phase shift to be recovered. Since this phase shift can be related directly to the electrostatic potential and the in-plane component of the magnetic induction in the sample, an electron hologram can be interpreted to provide quantitative information about electromagnetic fields with a spatial resolution approaching the nanometer scale. The development of the field-emission gun (FEG) as an electron source for the TEM has facilitated the practical implementation of electron holography in commercially available instruments, stimulating widespread interest and activity in the technique. One particular advantage of electron holography is that unwanted contributions to the

contrast that are caused by local variations in composition and sample thickness can, in principle, be removed from a recorded phase image. Electron holography has recently been applied to the characterization of a wide variety of nanostructured materials, including semiconductor devices and quantum well structures, as well as magnetic thin films and nanostructures.

This chapter provides a review of the application of off-axis electron holography to the characterization of electric and magnetic fields in nanostructured materials, which invariably behave differently from bulk structures. The chapter begins with a description of the experimental and theoretical basis of the technique. Applications of off-axis electron holography to nanostructured materials are then briefly reviewed. Examples of electrostatic fields that are described include electrostatic potentials associated with semiconductor junctions and layered structures, as well as the measurement of fringing fields around field-emitting carbon nanotubes. The characterization of nanoscale magnetic materials is then described. Results presented include nanopatterned elements and nanocrystalline chains. The interested reader is referred to several books [2–4] and review papers [5–8] for information about the development of electron holography and further applications of the technique that are beyond the scope of this chapter.

2. DESCRIPTION OF OFF-AXIS ELECTRON HOLOGRAPHY

2.1. Experimental Set-Up

More than 20 variants of electron holography have been identified [9]. By far the most fruitful of these has been off-axis electron holography which is illustrated schematically in Fig. 1. A high-brightness FEG electron source provides highly coherent electron illumination incident onto the sample. The region of interest is then positioned so that it covers approximately half of the field of view. A positive voltage, typically between 50 and 250 V, is applied to the electrostatic biprism, causing overlap between the wave that has passed through the sample with the vacuum (or reference) wave. The spacing of the resulting interference fringes is inversely proportional to the biprism voltage, and the total number of fringes is roughly proportional to the square of the biprism voltage.

A representative off-axis electron hologram from a chain of nanoscale magnetite crystals is shown in Fig. 2(a). The field of view is covered by two sets of fringes. The coarser fringes at the edges of the pattern are Fresnel fringes that originate from the edges of the biprism wire, whereas the finer fringes visible across almost the entire field of view are the holographic interference fringes. The relative changes in position and intensity of these holographic fringes can be interpreted to provide details about the phase shift and the amplitude, respectively, of the electron wave that has passed through the sample. The actual hologram reconstruction process is described in the next section.

Note that many of the results described here, such as the example shown in Fig. 2(a), have been acquired using a special minilens located below the normal objective lens, with this latter lens switched off so that the sample was located in a field-free environment. The lower magnification associated with this configuration is sufficient for

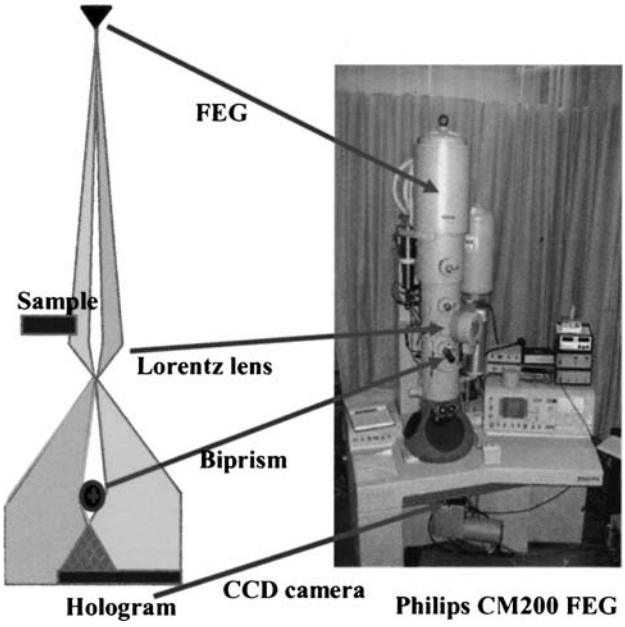

Figure 1. (Left) Schematic illustration of microscope configuration for off-axis electron holography. Field-emission-gun (FEG) electron source provides coherent electron beam incident on sample. Electrostatic biprism below sample causes overlap of vacuum (reference) wave with object wave. Modulations of hologram interference fringes recorded on CCD camera are interpretable in terms of phase/amplitude changes due to sample. (Right) Photograph of Philips CM-200 transmission electron microscope equipped with FEG electron source, a special Lorentz minilens beneath the normal objective lens enabling field-free observation of magnetic samples, an electrostatic biprism and a CCD camera for quantitative recording of holograms.

most magnetic samples, and provides an advantageous field of view for a variety of semiconductor applications.

2.2. Basic Imaging Theory and Hologram Reconstruction

Imaging in the TEM can be considered in terms of the modification of the incident electron wavefunction, first by the object, and then by the imaging objective lens. The intensity of the final image is found from the modulus squared of the resulting wavefunction [10].

At the exit-surface of the sample, the wavefunction can be expressed in the form

$$\Psi_s(\mathbf{r}) = A_s(\mathbf{r})\exp[i\phi_s(\mathbf{r})] \tag{1}$$

where A and ϕ are the amplitude and phase and $\mathbf{r}$ is a two-dimensional vector in the plane of the sample. The corresponding wavefunction at the image plane can be written

$$\Psi_i(\mathbf{r}) = A_i(\mathbf{r})\exp[i\phi_i(\mathbf{r})] \tag{2}$$

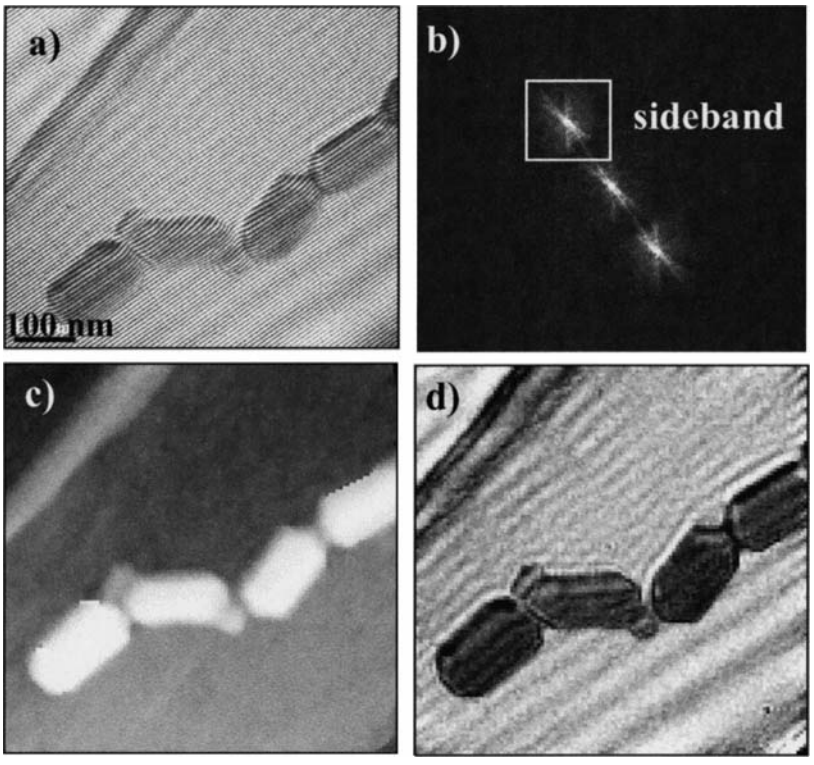

Figure 2. (a) Off-axis electron hologram showing chain of magnetite nanocrystals; (b) Fourier transform of (a), also indicating sideband used for reconstruction of complex image wave; (c) reconstructed phase image; (d) reconstructed amplitude image.

and the recorded intensity distribution is given by the expression

$$I(\mathbf{r}) = |A_i(\mathbf{r})|^2 \tag{3}$$

For a perfect thin lens, neglecting magnification and image rotation, the complex image wave $\Psi_i(\mathbf{r})$ can be regarded as equivalent to the object wave $\Psi_s(\mathbf{r})$.

In practice, unavoidable aberrations of the normal objective lens cause additional modifications to the phase and amplitude. These modifications can be represented by a phase-contrast transfer function, which takes the form

$$T(\mathbf{q}) = B(\mathbf{q})\exp[i\chi(\mathbf{q})] \tag{4}$$

where $B(\mathbf{q})$ is an aperture function in the focal plane of the objective lens, and the effects of the defocus, Δz, and spherical aberration, C_s, are included in the phase factor

$$\chi(q) = \pi \Delta z \lambda q^2 + \frac{\pi}{2} C_s \lambda^3 q^4 \tag{5}$$

The complex wavefunction in the image plane can then be written

$$\psi_i(\mathbf{r}) = \psi_s(\mathbf{r}) \otimes t(\mathbf{r}) \tag{6}$$

where $t(\mathbf{r})$ is the inverse Fourier transform of $T(\mathbf{q})$. The convolution, $\otimes$, of the object wave $\psi_s(\mathbf{r})$ with $t(\mathbf{r})$ represents an effective loss of resolution due to the lens aberrations. The intensity in the image plane can then be expressed in the form

$$I(\mathbf{r}) = A_i^2 = |\psi_s(\mathbf{r}) \otimes t(\mathbf{r})|^2 \tag{7}$$

Because of the phase oscillations introduced by $\chi(\mathbf{q})$, the image intensity is no longer related easily to the object structure. Thus, an accurate knowledge of the lens aberrations and imaging parameters is essential for high-resolution applications of electron holography.

An expression for the intensity distribution in an off-axis electron hologram can be obtained by adding a plane reference wave to the complex object wave in the image plane, with a tilt angle of $\mathbf{q} = \mathbf{q_c}$. Thus,

$$I_{\text{hol}}(\mathbf{r}) = |\psi_s(\mathbf{r}) \otimes t(\mathbf{r}) + \exp[2\pi i q_{\mathbf{c}} \bullet \mathbf{r}]|^2 \tag{8}$$

$$= 1 + A_i^2(\mathbf{r}) + 2A_i(\mathbf{r}) \cos[2\pi i q_c \bullet \mathbf{r} + \phi_i(\mathbf{r})] \tag{9}$$

i.e., the hologram intensity is the sum of three terms: the intensities of the reference and image waves, and an additional set of cosinusoidal fringes having phase shifts ϕ_i and amplitudes A_i that are equivalent to the corresponding phases and amplitudes, respectively, of the image wave. These fringes correspond to the fine interference fringes that are spread across the field of view in Fig. 2(a).

The recorded hologram must be "reconstructed" in order to extract the required phase and amplitude information from the complex image wave. The hologram is first Fourier-transformed, which can be accomplished either optically or, preferably, digitally for reasons that are explained further below. This procedure is described by the equation

$$FT[I_{\text{hol}}(\mathbf{r})] = \delta(\mathbf{q}) + FT[\mathrm{A}_i^2(\mathbf{r})] \tag{10a}$$

$$+ \delta(\mathbf{q} + \mathbf{q_c}) \otimes [A_i(\mathbf{r}) \exp[i\phi_i(\mathbf{r})]] \tag{10b}$$

$$+ \delta(\mathbf{q} - \mathbf{q_c}) \otimes [A_i(\mathbf{r}) \exp i\phi_i(\mathbf{r})]] \tag{10c}$$

This expression contains four terms: the central peak at the origin corresponds to the Fourier transform of the uniform intensity of the reference image, a second peak centered at the origin represents the Fourier transform of the conventional TEM micrograph of the specimen, and the remaining two peaks centered on $\mathbf{q} = -\mathbf{q_c}$ and $\mathbf{q} = +\mathbf{q_c}$ constitute the desired image wavefunction, and its complex conjugate. In the Fourier transform of the hologram shown in Fig. 2(b), these various contributions are visible as the central "auto-correlation" peak and two "sidebands". The two sidebands contain identical information except for a change in the sign of the phase.

The final part of the hologram reconstruction procedure involves using an 'aperture', as shown in Fig. 2(b), to select one of the sidebands, which is then inverse-Fourier transformed. The sideband region must be separated from the central peak by choosing a small enough fringe spacing, and by selecting the size of the aperture, which is usually square, but can be rectangular, depending on the object being studied [11]. The reconstructed phase and amplitude images from Fig. 2(a) are shown in Figs. 2(c) and 2(d), respectively.

2.3. Phase Shifts and Mean Inner Potential

The electrons that pass through a TEM sample undergo phase shifts that depend on the electrostatic potential and the in-plane component of the magnetic induction. Neglecting dynamical diffraction effects, the phase shift can be expressed in the form [12]

$$\phi(x) = C_E \int V(x, z)\, dz - \left(\frac{e}{\hbar} \iint B_\perp(x, z) t(x)\, dx\, dz\right) \tag{11}$$

where z is the incident electron beam direction, x is a direction in the plane of the sample, V is the electrostatic potential, $B_\perp$ is the component of the magnetic induction in the sample perpendicular to both x and z, and C_E is an energy-dependent constant that has the value of 7.28×10^{-3} rad/V·nm at an electron accelerating voltage of 200 kV.

When neither V nor $B_\perp$ vary within the sample along the beam direction, then equation (11) can be simplified to

$$\phi(x) = C_E V(x) t(x) - \left(\frac{e}{\hbar}\right) \int B_\perp(x) t(x)\, dx \tag{12}$$

where t is the sample thickness. Differentiation with respect to x then yields

$$\frac{d\phi(x)}{dx} = C_E \frac{d}{dx} \{V(x) t(x)\} - \left(\frac{e}{\hbar}\right) B_\perp(x) t(x) \tag{13}$$

In a sample of uniform thickness and composition, the first term in this expression is zero, and the phase gradient is directly proportional to the in-plane component of the magnetic induction

$$\frac{d\phi(x)}{dx} = \left(\frac{et}{\hbar}\right) B_\perp(x) \tag{14}$$

By adding contours to the phase image, a direct representation of the magnetic induction in the sample is obtained. Phase differences of 2π between adjacent contours correspond to steps of $\int \mathbf{B} \cdot d\mathbf{S} = (h/e) = 4 \times 10^{-15}$ Wb, thus allowing magnetic fields to be measured and quantified on an absolute basis [8].

The mean inner potential (MIP) of the sample, V_0, which depends on the local composition and density, is usually the dominant contribution to the electrostatic potential. The MIP is defined as the volume average, or the zeroth-order Fourier coefficient, of the electrostatic potential [13]. For low-energy electrons, the MIP varies with the energy of the incident electrons [14], whereas the MIP measured using high-energy electrons [15] can be regarded as a fundamental property of the material.

In the absence of magnetic and long-range electric fields, such as those occurring at depletion regions in semiconductors, and assuming that dynamical diffraction can be neglected, then equation (11) can be re-written

$$\phi(x) = C_E \int V_0(x, z)\, dz \tag{15}$$

If the sample has uniform structure and composition in the beam direction, then this expression reduces still further to

$$\phi(x) = C_E V_0(x) t(x) \tag{16}$$

These expressions ignore multiple scattering within the sample, and therefore only apply to crystalline samples when they are tilted to weakly diffracting orientations.

Electron holography provides the most accurate technique currently available for measuring the sample MIP, by using equation (16) and making use of experimental phase profiles. The most straightforward approach is to use a cleaved wedge so that the thickness changes in a well-defined manner as a function of distance from the edge of the sample [16]. The MIP can also be determined by measuring the gradient of the phase $d\phi/dx$, and using the relation

$$V_0 = \left(\frac{1}{C_E}\right)\left(\frac{d\phi/dx}{dt/dx}\right) \tag{17}$$

The advantage of this approach is that it is independent of any contributions to the phase shift from amorphous overlayers on the sample surface, since $dt/dx = 0$ when these layers are of uniform thickness.

Dynamical corrections to the phase always need to be taken into account when determining V_0 from any crystalline sample, including a cleaved wedge. These corrections are necessary even when the electron hologram has been acquired at a weakly diffracting condition. For greatest possible accuracy, the exact orientation of the crystalline sample should be recorded using a technique such as convergent-beam electron diffraction, and the dynamical contributions should then be simulated at this angle [16, 17]. An independent measure of the sample thickness is highly recommended. Dynamical corrections to V_0 are typically between 0.1 and 0.2 V even at weakly diffracting orientations [18]. Values of the MIP measured for a wide range of materials have been compiled [17].

2.4. Quantification

Traditionally, the reconstruction of electron holograms has been carried out 'optically' using a laser bench [6]. Electron holography has recently benefitted greatly from the use of quantitative recording [19], and the charge-coupled-device (CCD) camera is nowadays the standard medium of choice for recording holograms. These devices have a linear response over several orders of magnitude, they have high detection quantum efficiency, and the recorded information is immediately accessible for digital processing [20]. Moreover, fast and inexpensive computers and sophisticated software [21] are now readily available. Digital reconstruction of holograms using computer processing has thus become widespread.

Off-axis electron holography relies on information stored in the lateral displacement of interference fringes, and thus distortions in the recording medium are liable to cause displacements that could be misinterpreted. The reconstructed phase image may have long-range modulations due to several factors, which include distortions caused by the projector lenses and the recording system, and inhomogeneities in the charge and thickness of the biprism wire. Since these distortions are usually geometrical in nature and invariant in time, their effects can be removed by the simple procedure of recording a reference hologram with the sample removed from the field of view but without any changes to the optical parameters of the microscope. Correction is then carried out by a complex division of the reconstructed (sample and reference) image waves in real space, giving the required distortion-free phase of the image wave [19, 22]. Relative phase changes within the sample can then be interpreted faithfully.

The interference-fringe spacing and the spatial resolution of the phase image depend on several geometrical factors as well as the biprism voltage and the imaging lenses [23, 24]. The phase detection limit depends on the signal-to-noise ratio in the phase image, which may be low if the recorded signal is of low intensity [25]. Since off-axis electron holograms are typically recorded at electron doses of 100–500 electrons per pixel, the recording process is dominated by Poisson noise [26]. The quality of the hologram depends on the characteristics of the recording medium (CCD camera), as well as on the fringe visibility (or contrast), which depends in turn on the illumination diameter and the biprism voltage. Loss of fringe contrast will result from the finite source size, the beam energy spread, stray electrostatic and magnetic fields, and the mechanical stability of the biprism wire.

A major problem with the digital reconstruction of phase images is that they are usually evaluated modulo 2π, meaning that 2π phase discontinuities that are unrelated to specimen features appear at positions where the phase shift exceeds this amount. Phase "unwrapping" using suitable algorithms is then required before reliable interpretation of image features becomes possible. Several phase unwrapping algorithms are available for the purpose of locating and unwrapping such discontinuities, but none of these are yet able to solve all of the problems. The most straightforward approach involves searching the image row-by-row or column-by-column for adjacent pixels with phase differences that exceed a pre-selected value, and then adding or subtracting 2π to the subsequent pixels. Alternatively, a second phase image may be calculated

after multiplying the complex image wave by a phase factor $\exp(i\alpha)$ to move the phase jumps to different places in the image [27]. Advanced phase-unwrapping techniques [28] are now being introduced into the software that is used to analyze electron holograms. These and other issues relating to hologram quantification have been discussed in more detail elsewhere [29].

2.5. Practical Considerations

Electron holography requires highly coherent incident illumination, which suggests that large source demagnifications are necessary. However, the use of rotationally symmetric illumination is not advantageous since a significant improvement in coherence can be achieved by employing highly elliptical illumination. The condensor lens stigmators and focus settings are then adjusted to produce elliptical illumination at the sample level that is elongated in the direction perpendicular to the biprism wire when the condensor lens is overfocused, but relatively narrow in the parallel direction. Illumination aspect ratios of 50–100 are common for medium-resolution electron holography [30].

A severe practical limitation of off-axis electron holography is the requirement for a (vacuum) reference wave that can be overlapped onto the region of interest. Thus, off-axis electron holograms must usually be recorded from near the edge of the specimen. For high-resolution applications, which require very high sampling density, this requirement can represent a severe restriction on the size of the useful specimen regions that can be examined. For medium resolution applications, the region of interest and the reference wave can typically be separated by no more than a few microns at the very most. This restriction can be relaxed in the special case of a sample that has a thin and featureless region of electron-transparent support film, rather than vacuum, which can be overlapped onto the specimen feature of interest.

When examining magnetic materials, the conventional objective lens must be switched off, since its strong vertical field would otherwise saturate the magnetization of the sample in the electron beam direction. It is common to use a high-strength 'Lorentz' minilens located beneath the sample to provide high magnifications with the sample located in a field-free environment [31]. At the same time, a larger fringe overlap width of 1–2 μm can be obtained, with typical interference fringe spacings in the range of 1–5 nm. It should also be appreciated from equations (11) and (12) that the total phase shift for a nanostructured magnetic material will be dominated by the mean inner potential. The magnetic contribution to the phase is approximately proportional to the width of the particular magnetic element unlike the MIP contribution which is independent of its lateral dimensions. Thus, accurate quantification of the magnetic contribution to the phase becomes more challenging for elements of narrow width. Separation of the two contributions can be achieved in several ways [8]. Inversion of the sample in the microscope, which is inconvenient and not usually straightforward, would change the sign of the magnetic contribution to the phase. Subtraction of the two respective phase images would allow the MIP contribution to the phase to be removed. Alternatively, it is often possible to achieve magnetization reversal by tilting

the sample *in situ* with the main objective lens slightly excited, again enabling the MIP contribution to be measured and then removed from other phase images [32]. This possibility proves to be highly useful when tracking magnetization reversal processes during entire hysteresis cycles.

3. NANOSCALE ELECTROSTATIC FIELDS

Detailed knowledge of the electrostatic potential distribution within semiconductor materials is vital to a full understanding of device performance, in particular to account for offsets that occur at heterojunctions and extended defects, such as charged dislocations. Band-bending at interfaces, in conjunction with the presence of extrinsic dopants, determines electron transport, and effectively controls device operation. The depletion field at a simple p–n junction is well-established theoretically [33], but techniques that can be used to map potential distributions across complex heterojunctions at the nanometer scale are generally unavailable. As device dimensions are further reduced into the deep-submicron regime, methods that are capable of quantitatively determining two-dimensional dopant concentration profiles with the required precision and spatial resolution become even more crucial. Off-axis electron holography is uniquely capable of accessing and quantifying nanoscale electrostatic fields. This section describes several areas where the technique has already had a substantial impact.

3.1. Dopant Profiles

Electron holography is potentially a valuable method for investigating semiconductor junctions and devices. Early low-resolution investigations of p–n junctions by electron holography revealed an electrostatic fringing field outside a biased sample [34]. We were later able to measure directly the intrinsic electrostatic potential distribution across a p- and n-doped Si/Si junction [35]. These initial results were limited in precision by signal-to-noise considerations and sample preparation methods. Much improved precision and spatial resolution have since been achieved by making use of the enhanced stability and higher electron beam coherence available with a modern FEG-TEM [36, 37]. The reconstructed hologram of a p-type field-effect transistor, which is shown in Fig. 3, illustrates this improved capability. This particular application demonstrates two-dimensional imaging of electrostatic potential distributions across devices with a sensitivity closely approaching 0.15 V and spatial resolution approaching 6 nm. Such information about doped heterojunctions is invaluable for evaluating and refining competing models for dopant diffusion.

Practical difficulties still prevent electron holography from being used routinely in device characterization. The most serious problem relates to the preparation of a uniformly thinned cross-section of the region of interest, which must also be located close to the sample edge because electron holography requires an unperturbed reference wave to facilitate phase reconstruction. Focused-ion-beam (FIB) milling is widely used in the semiconductor industry for thinning specific sample sites. However, residual Ga implanted inadvertently during FIB milling results in a surface "dead" layer [38], which decreases the potential measured by electron holography. Additional steps such

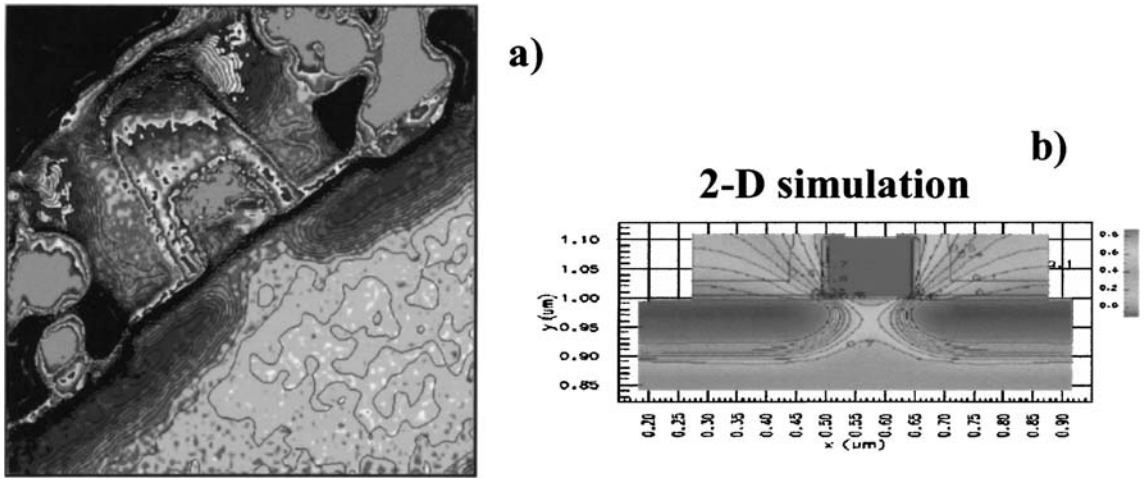

Figure 3. (a) Reconstructed off-axis electron hologram of electrostatic potential variation associated with 0.13-μm p-type field-effect transistor; and (b) corresponding simulated 2-D potential map. Phase contours of 0.1V [37]. (See color plate 18.)

as reverse biasing of the sample may then be required before reliable results can be obtained using electron holography [39].

Surface damage and depletion at the top and bottom surfaces of doped samples prepared using routine ion-milling has also been reported to create electrically "dead" layers [40], with typical thicknesses of ~25 nm. By using wedge polishing followed by low-angle, low-energy milling, we were able to mitigate these effects and obtain high measurement precision [36, 37, 41]. However, for many applications involving the characterization of 2-D dopant distributions, access to the region of interest for holography study can most conveniently be achieved only by using FIB milling. Surface depletion effects arising from sample preparation then become unavoidable and must be taken into account.

3.2. Piezoelectric Fields

Another area of recent interest and activity involving the application of off-axis electron holography to the characterization of nanoscale electrostatic fields has been the study of nitride semiconductors, which are important candidates for a range of novel optoelectronic applications [42]. For example, large internal piezoelectric fields of ~1 MV/cm have been observed in strained GaN/InGaN/GaN quantum wells [43]. Such piezoelectric fields, in addition to the spontaneous polarization field, play a major role in proposed device applications of Group III-nitride materials [42]. These fields result from the pseudomorphic growth of highly strained Ga(In)N/GaN and Ga(Al)N/GaN quantum well (QW) structures in the polar [0001] direction. Electron holography has been used in recent studies [43–46] to quantify the electrostatic potential profiles across strained QW heterostructures grown without intentional doping. Features in the measured potential profiles have been variously attributed to the accumulation of sheet charge [44, 45] and the presence of a two-dimensional gas (2DEG) near the heterointerface [46]. In our study of the electrostatic potential variation across an n-AlGaN/InGaN/p-AlGaN heterojunction diode by off-axis electron holography, we have shown that it is also possible to account for the additional effects that are caused by the overlapping built-in potential of the pn junction [47]. Figure 4(a) compares the experimental profile with the separate contributions to the electrostatic energy profile simulated for the p–n junction, V_{pn}, the spontaneous polarization, V_{sp}, and the piezoelectric field, V_{pe}. Figure 4(b) then compares the experimental profile (open circles) with a simulated profile that incorporates the piezoelectric and spontaneous polarizations, as well as the effects of charge accumulation at the n-AlGaN/InGaN and InGaN/p-AlGaN interfaces. The close agreement between the experimental and simulated profiles provides strong evidence for the presence of sheet charge at these interfaces.

3.3. Charged Defects

Optoelectronic devices based on Group III-nitride semiconductors are becoming widespread and recent activity has been directed towards improving device lifetimes and light-emitting efficiency [40]. However, fundamental questions remain unanswered or

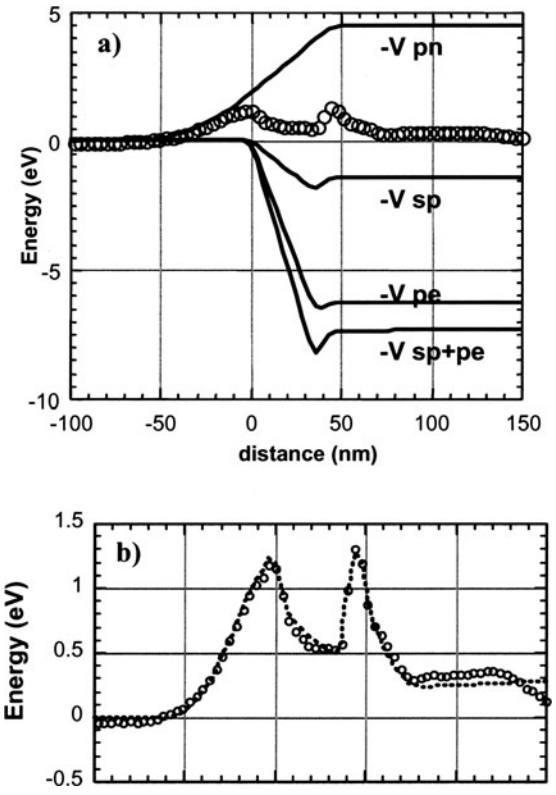

Figure 4. Analysis of electrostatic potential profile across n-AlGaN/InGaN/p-AlGaN heterojunction diode. (a) Energy profile derived from thickness-corrected phase image (open circles) for comparison with individual contributions from p–n junction, V_{pn}, spontaneous polarization, V_{sp}, and piezoelectric filed, V_{pe}. (b) Experimental energy profile (open circles) across heterojunction diode compared with simulation (dotted line) incorporating spontaneous and piezoelectric polarization as well as sheet charge at each interface [47].

results are ambiguous relating to the charge state of the ubiquitous threading dislocations found in these materials, and their effect on device performance. Electron holography has been used in attempts to resolve these issues by measuring electrostatic potential profiles across different types of dislocations [48–50]. The charge density can then be calculated by using Poisson's equation [51]. For example, based on electron holography observations, it was reported that the core regions of screw, mixed and edge dislocations in undoped GaN were negatively charged [48], whereas it was concluded from other holography studies that dislocation cores in n-GaN and p-GaN were, respectively, negatively [49] or positively [50] charged. However, these latter results have been contradicted by subsequent observations made using scanning surface potential microscopy where defects in Si-doped p-type GaN were reported to be electrically neutral [52]. Studies made using ballistic electron emission microscopy found

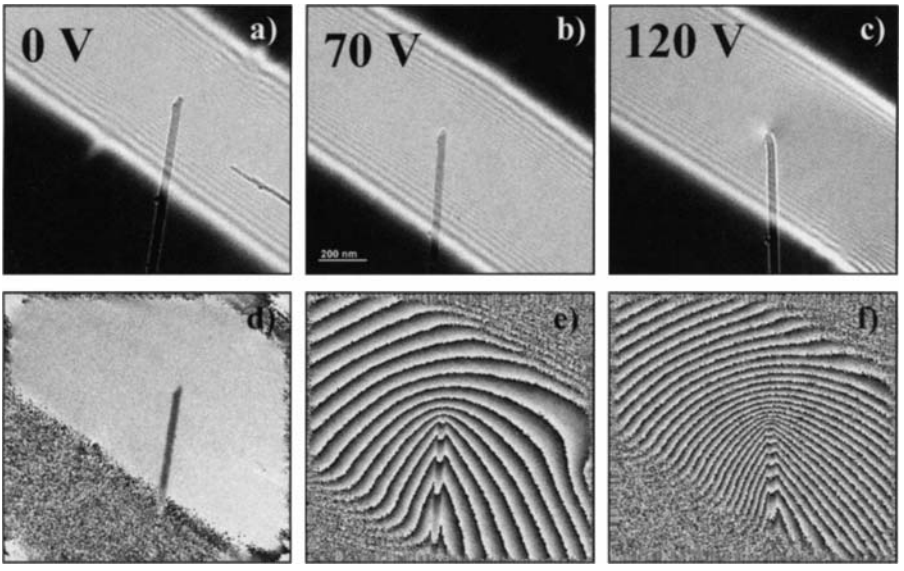

Figure 5. Observation of field-emitting carbon nanotube using off-axis electron holography: (a), (b), and (c) Electron holograms of carbon nanotube at bias voltages $V_B = 0$, 70, and 120 V, respectively. (d), (e), and (f) reconstructed phase images corresponding to (a), (b) and (c), respectively. Phase contour separation of 2π radians. Phase gradient in (f) corresponds to electric field strength at tip of 1.22 V/nm [55].

no evidence for negative dislocation charge [53]. It is conceivable that these differences result from TEM sample preparation or surface charging artefacts, or because localized strain or sample thickness variations around the dislocation core regions affects the diffraction conditions and the measured holographic phase contrast. Further systematic studies of extended defects by electron holography are required, first to eliminate these possibilities, and second to determine whether defect charging is associated with the nitride growth conditions or with the level and type of doping.

3.4. Field-Emitting Carbon Nanotubes

Single-walled and multi-walled carbon nanotubes are attracting much recent attention because of their remarkable resilience, strength and thermal conductivity [54]. The use of carbon nanotubes in arrays of field emitters is of particular interest for compact displays. Electron holography has been used to determine the electrostatic potential distribution associated with individual field-emitting carbon nanotubes [55]. A specially constructed, piezo-driven sample manipulation stage enabled nanotubes to be positioned several microns away from a small collector plate. A variable bias voltage could then be applied between the nanotubes and the plate, as off-axis electron holograms were acquired. Figure 5 shows a sequence of electron holograms from a carbon nanotube and the corresponding reconstructed phase images for bias voltages of 0, 70 and 120 V. The onset of field emission for this nanotube occurred at a threshold bias

voltage close to 70 V. The closely spaced 2π phase contours in Fig. 5(c) reflect the extremely high electric field in the vicinity of the field-emitting tip during electron emission. A model based on a one-dimensional line of charge established that the electric field was concentrated at the tip of the nanotube. The field strength was calculated to be 1.22V/nm in close agreement with the experimental phase image.

3.5. Thickness and Sample Morphology

The phase image, as described by equation (16), represents a map of the projected sample thickness if the MIP is constant, and dynamical scattering is weak. Hence, it is then possible under these special circumstances to infer the surface topography and the shapes of nanoparticles using electron holography. For example, line profiles across reconstructed phase images have been used to deduce surface structures and to identify internal voids in small Pd particles [56] and cuboctahedral ZrO_2 particles [57]. Further examples are summarized elsewhere [8].

An alternative approach for specimen thickness determination makes use of the amplitude image, through the equation

$$t(x) = -2\lambda_{\text{in}} \ln\left(\frac{A_s(x)}{A_r(x)}\right) \tag{18}$$

where λ_{in} is the mean-free-path for inelastic scattering, and $A_s(x)$ and $A_r(x)$ are the measured amplitudes of the sample and reference holograms, respectively [58]. A practical problem with this approach is that amplitude images are always noisier than the corresponding phase images. Moreover, λ_{in} will invariably be different for each material in the sample, and may be unknown. Most TEM samples do not have uniform thickness profiles, and thickness determination is not straightforward when the sample has non-uniform composition. Further analysis [59] reveals yet another approach that has enabled holograms from multilayered samples with varying compositions and unknown thickness variations to be successfully interpreted [60, 61].

4. NANOSCALE MAGNETIC FIELDS

Nanoscale magnetic materials have become increasingly important in many practical applications that include non-volatile storage media, electromechanical read/write devices and mechanical sensors [62]. The future of many magnetic devices lies in their capacity for higher storage density, which necessitates further reductions in the sizes of information blocks, and the simultaneous down-scaling of the distances between them. Some of the problems that result from reducing the device dimensions are obvious. First, the magnetic domain size becomes comparable to the mean bit size. Second, individual bits may interact with neighboring blocks by way of their stray fields. In order to improve the overall performance of devices based on magnetic materials, the local microstructure and chemical composition must be tailored to optimize the magnetic properties on the nanometer scale. There are many electron microscopy techniques that are suitable for the characterization of magnetic microstructure [63], but only electron holography allows the quantification of magnetic fields in nanostructured

materials at the nanometer scale. An extensive bibliography summarizing applications of the technique to magnetic materials can be found elsewhere [8]: this section provides a brief overview of some representative applications that are relevant to nanotechnology.

4.1. Patterned Nanostructures

Magnetic interactions between closely-spaced, submicron-sized magnetic elements depend sensitively on their shape, size, composition and spacing. The characterization of such interactions is of great importance if nanoscale magnetic materials are to be used in future magnetic recording and sensing applications. Such applications usually require specific values of the coercive fields and remanent magnetizations of individual magnetic nanostructures, as well as stable and reproducible magnetic domain states. To gain insight into these important issues, we have used off-axis electron holography to observe an extensive range of patterned magnetic elements, which were prepared using electron-beam lithography and lift-off processes, and supported on electron-transparent silicon nitride membranes [32, 64–67]. The element shapes included rectangles with varying aspect ratios, as well as diamonds, ellipses and rectangular bars. The fabrication processes have been described in more detail elsewhere [32]. Magnetic fields were applied to each sample by *in situ* tilting within the microscope with the conventional objective lens slightly excited in order to obtain the desired in-plane magnetic fields. The hysteresis loops of the various element shapes could be followed, despite the substantial loss of interference-fringe contrast due to the presence of the underlying silicon nitride support.

Figure 6 shows the magnetic contributions to the measured holographic phase shift for two closely-spaced polycrystalline Co rectangles over a complete magnetization reversal cycle [64]. These holograms were recorded with an average out-of-plane field of 3600 Oe for the in-plane horizontal fields indicated on the figure. The separation of the phase contours is proportional to the in-plane component of the magnetic induction integrated in the incident beam direction. The magnetic fringing fields between the elements are only minimized when the field lines are located entirely within each element, in the flux closure (or solenoidal) vortex state.

An important aspect of these studies was the use of micromagnetic simulations, based on solutions to the Landau-Lifshitz-Gilbert equations, to assist with detailed interpretation of the experimental phase images [32, 65, 66]. Although reasonable agreement with the experimental results was obtained, important differences were also noticed. For example, simulated vortex states formed at higher fields than observed experimentally, which was attributed to the influence of local defects or inhomogeneities. Moreover, slight differences in the initial, nominally saturated, state had a strong effect on subsequent domain evolution during the reversal process. The strength and direction of the out-of-plane component of the applied field also had a marked impact on the observed domain structure [65]. The simulations in Figure 7 show a comparison of two elements simulated first as a pair (left set), and then separately (but displayed together). The marked difference in the domain configurations of the smaller cell on the left

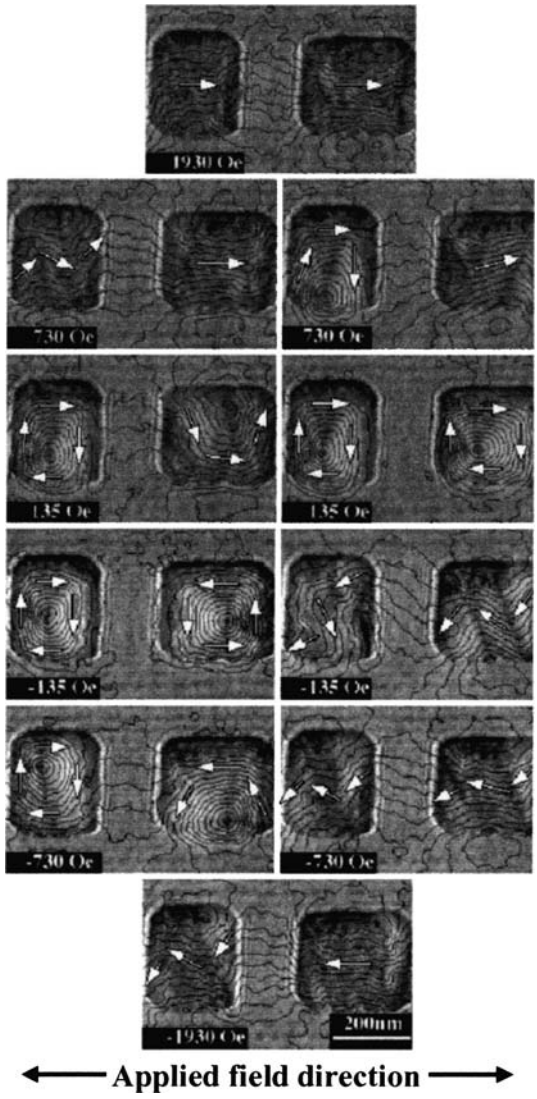

Figure 6. Magnetic contributions to phase for 30-nm-thick Co nanopatterned elements recorded during complete hysteresis cycle by tilting *in situ* within the microscope. In-plane magnetic field applied along horizontal direction as indicated. Average out-of-plane field of 3600 Oe directed into the page. Phase contours separated by 0.21π radians. Loop should be followed in counter-clockwise direction [64].

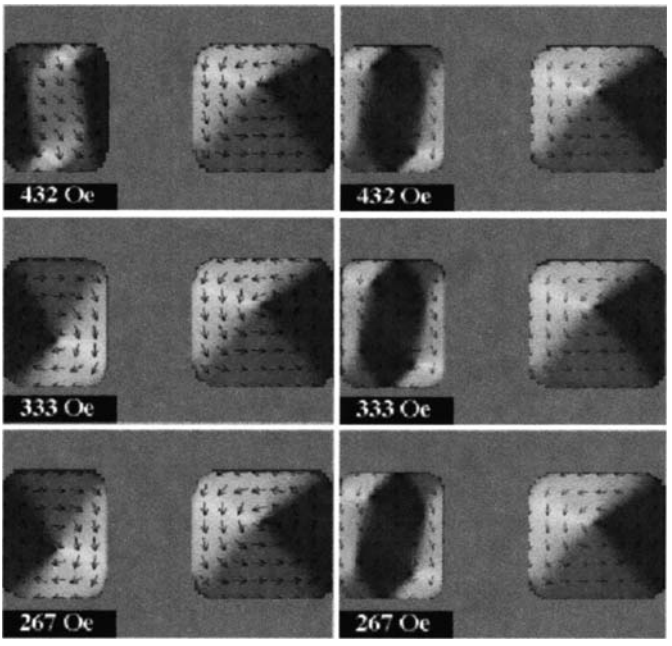

Figure 7. Micromagnetic simulations for 30-nm-thick Co elements with 3600 Oe vertical field directed into the page. Left set simulated for two cells together, whereas right set simulated for each cell separately (though shown together). Differences visible in small element at left due to close proximity of larger element [65].

clearly indicate that these adjacent Co elements are affected by their close proximity. This study emphasizes the importance of comparing experimental measurements with micromagnetic simulations. Interactions between closely-spaced magnetic nanostructures are clearly important for the design of high-density magnetic storage devices.

While these results for nanopatterned Co elements are of considerable scientific interest, the behavior of multilayered elements is of much greater relevance for many practical applications because of the large resistance changes that occur when two closely-spaced magnetic layers have either parallel or anti-parallel magnetization directions (an effect known as giant magnetoresistance [68]). Our further studies focused on submicron "spin-valve" (SV) elements consisting of Co (10 nm)/Au (5 nm)/Ni (10 nm) layers. The SV elements were shaped as rectangles, diamonds, ellipses and bars [66, 67]. Hysteresis loops for individual elements were measured experimentally, based on the density and direction of the phase contours, and compared with loops derived from micromagnetic simulations. Differences in switching fields between the data and the simulations were observed in smaller elements, possibly due to an increased practical difficulty in nucleating end domains that could initiate magnetization reversal. Another significant observation was the direct observation of two different phase spacings in different remanent states in each element. Micromagnetic simulations established that parallel or anti-parallel coupling between the Co and Ni layers was the cause of this

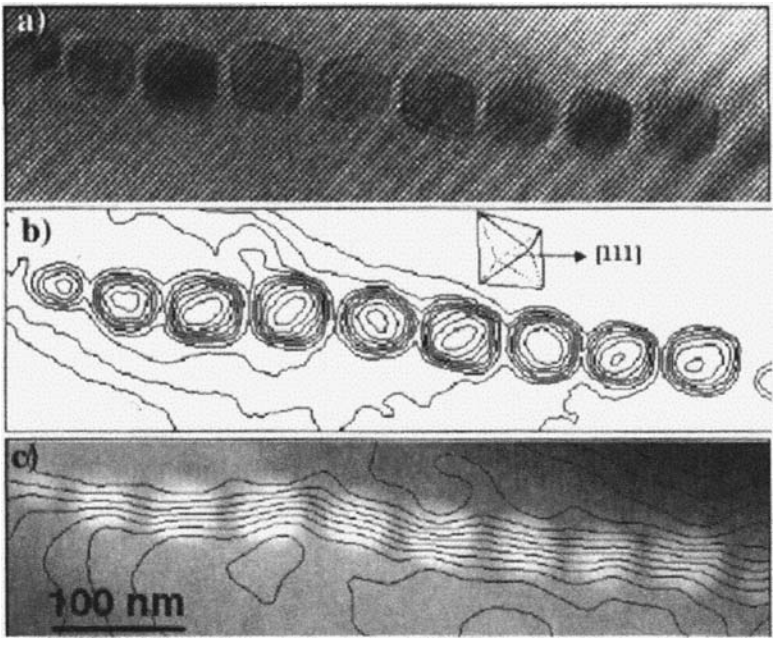

Figure 8. (a) Hologram of chain of magnetite nanocrystals from *magnetospirillum magnetotacticum*; (b) mean inner potential contribution to phase of reconstructed hologram. Thickness contours indicate that magnetite crystals have cuboctahedral shape. (c) magnetic contribution to phase.

behavior. The Ni layer in each element was found to reverse its magnetization direction well before the external field was removed due to the strong fringing field of the closely adjacent and magnetically more massive Co layer. Thus, an antiferromagnetically coupled state was always observed as the remanent state following the removal of the external field. Solenoidal states were observed experimentally for both elliptical- and diamond-shaped elements but could not be reproduced in the simulations, presumably because these states were stabilized by the presence of structural imperfections, or by the crystal grain size or crystallographic texture of the polycrystalline layers.

4.2. Nanoparticle Chains

The formation of reproducible remanent states when an applied external field is removed is desirable for nanopatterned magnetic elements intended for device applications. Because of their geometry, chains of nanocrystalline magnetic particles lend themselves to unidirectional remanent states. Moreover, magnetostatic effects in electon holographic phase images can be separated from those due to thickness and electrostatic effects simply by *in situ* tilting of the sample in the field of the conventional objective lens to achieve magnetization reversal.

Linear chains of ferrimagnetic crystals, known as magnetosomes, are contained in magnetotactic bacteria [69]. Figure 8 shows an off-axis electron hologram of a chain of

magnetite crystals in a single cell of the bacterial strain *Magnetospirillum magnetotacticum*. After magnetization reversal, the MIP contribution to the phase shift can be identified, as shown in Fig. 8(b). The crystallites in this image are revealed by the thickness contours to have cuboctahedral shapes [70]. The corresponding magnetic contributions to the phase shifts, achieved by subtracting the respective pairs of holograms, are shown in Fig. 8(c). Phase contours have been overlaid onto the MIP contribution allowing the positions of the crystals and the magnetic contours to be correlated with each other. The magnetic flux within and between the crystallites can be clearly visualized. Moreover, it is straightforward to obtain an estimate for the total magnetic dipole moment of the particle chain by measuring the step in the magnetic contribution to the phase shift across the chain, as described elsewhere [8]. Further studies of several strains of magnetotactic bacteria have revealed chains of crystals that form either single magnetic domains [71], or else more complicated domain structures in larger magnetosomes [72].

In contrast, chains of FeNi nanoparticles, which have variable sizes, spherical geometry, and a mean diameter of 50 nm, show markedly different behavior [73]. Closely-spaced phase contours are observed to channel through several particles along such chains. Some very interesting domain structures arise, primarily due to the variability of the particle sizes and their relative positions, both along the chain and with respect to the chain axis. The key result, which is illustrated by the examples shown in Fig. 9 and confirmed by micromagnetic simulations, is the formation of three-dimensional magnetic vortices with complex geometries that are determined by the particle sizes and locations. These results emphasize yet again the necessity for controlling the shapes, sizes, and relative locations of closely-separated magnetic nanoparticles, and for understanding their mutual interactions.

5. FUTURE PERSPECTIVES

Off-axis electron holography has evolved over the years to the extent that it can be considered as a routine and reliable technique for characterizing nanostructured materials. As the dimensions of magnetic storage and electronic devices continue to shrink still further, electron holography will provide an increasingly valuable approach for solving industrial problems, as well as for providing advances in fundamental scientific knowledge. Unique information about nanoscale electrostatic and magnetic fields is readily obtainable, and quantification on the same scale is often possible. A major restriction of the technique is that dynamic events cannot conveniently be followed in real time because of the need for off-line processing. However, there is some realistic prospect that faster recording systems and computers may overcome this limitation. The available field of view, which depends on the geometry and the dimensions of the imaging and recording systems (e.g., the width of the fringe overlap region, the sampling of the holographic fringes, and the finite size of the CCD array) can also represent a very real limitation for some applications. Nevertheless, the results described here and elsewhere indicate that the technique will become more and more heavily used in the burgeoning field of nanotechnology.

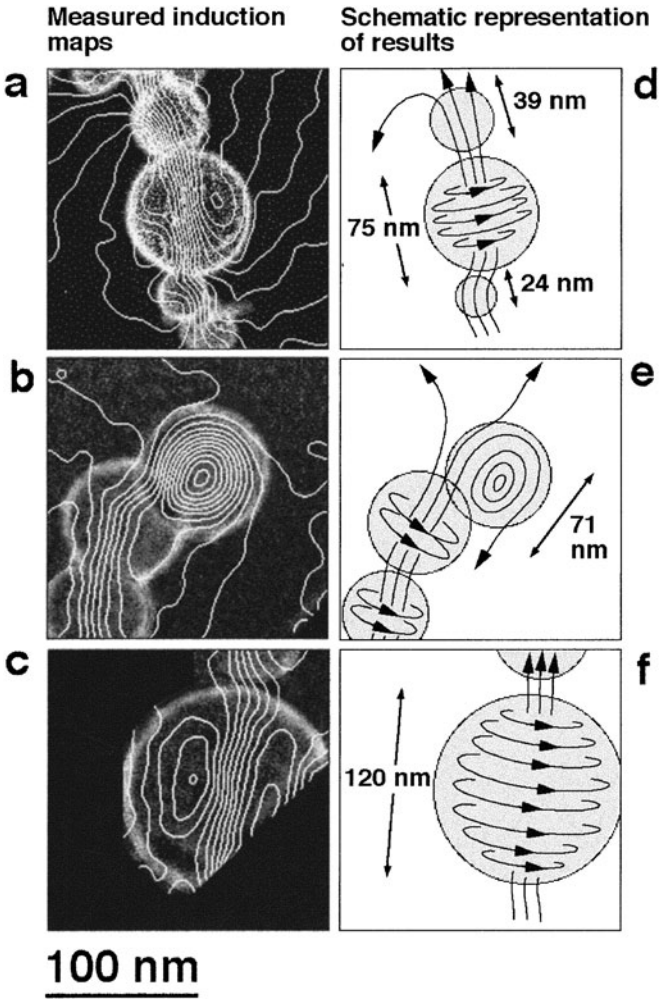

Figure 9. (a–c) Experimental phase contour maps along chains of FeNi nanoparticles after removal of mean inner potential contribution. Contour spacings of 0.083, 0.2, and 0.2 radians, respectively. (d–f) Schematic interpretation of magnetic microstructure, including magnetic vortices in each case [73].

REFERENCES

1. D. Gabor, *Proc. Roy. Soc. London*, A197 (1949) 454.
2. A. Tonomura, L. F. Allard, G. Pozzi, D. C. Joy, and Y. A. Ono (Eds.), *Electron Holography*, Elsevier, Amsterdam (1995).
3. E. Völkl, L. F. Allard, and D. C. Joy (Eds.), *Introduction to Electron Holography*, Plenum, New York (1998).
4. A. Tonomura, *Electron Holography*, Springer-Verlag, Berlin (1999).
5. H. Lichte, *Adv. Opt. Elect. Microsc.* 12 (1991) 25.
6. A. Tonomura, *Adv. Phys.* 41 (1992) 59.
7. P. A. Midgley, *Micron* 32 (2001) 167.

8. R. E. Dunin-Borkowski, M. R. McCartney, and D. J. Smith, In: *Encyclopedia of Nanoscience and Nanotechnology*, H. S. Nalwa (Ed.), American Scientific, Stevenson Ranch, CA (2004).
9. J. M. Cowley, *Ultramicroscopy* 41 (1992) 335.
10. J. M. Cowley, *Diffraction Physics*, Third Revised Edition, North Holland, Amsterdam (1995).
11. K. Ishizuka, *Ultramicroscopy* 51 (1993) 1.
12. L. Reimer, *Transmission Electron Microscopy*, Springer, Berlin (1991).
13. J. C. H. Spence, *Acta Cryst*, A49 (1993) 231.
14. M. A. van Hove, W. H. Weinberg, and C. M. Chan, *Low Energy Electron Diffraction*, Springer, Berlin (1986).
15. D. K. Saldin and J. C. H. Spence, *Ultramicroscopy* 55 (1994) 397.
16. M. Gajdardziska-Josifovska, M. R. McCartney, W. J. de Ruijter, D. J. Smith, J. K. Weiss, and J. M. Zuo, *Ultramicroscopy* 50 (1993) 285.
17. M. Gajdardziska-Josifovska and A. Carim, In: *Introduction to Electron Holography*, E. Völkl, L. F. Allard, and D. C. Joy (Eds.), Kluwer, New York (1998) pp. 267–293.
18. J. Li, M. R. McCartney, R. E. Dunin-Borkowski, and D. J. Smith, *Acta Cryst*. 55 (1999) 652.
19. W. J. de Ruijter and J. K. Weiss, *Ultramicroscopy* 50 (1993) 269.
20. W. J. de Ruijter and J. K. Weiss, *Rev. Sci. Inst*. 63 (1992) 4314.
21. W. O. Saxton, T. J. Pitt, and M. Horner, *Ultramicroscopy* 4 (1979) 343.
22. W. D. Rau, H. Lichte, E. Völkl, and U. Weierstall, *J. Comp-Assisted Microsc.* 3 (1991) 51.
23. H. Lichte, *Ultramicroscopy* 20 (1986) 293.
24. H. Lichte, *Ultramicroscopy* 51 (1993) 15.
25. A. Harscher and H. Lichte, *Ultramicroscopy* 64 (1996) 57.
26. H. Lichte, K.-H. Herrmann, and F. Lenz, *Optik* 77 (1987) 135.
27. D. J. Smith, W. J. de Ruijter, M. R. McCartney, and J. K. Weiss, In: *Introduction to Electron Holography*, E. Völkl, L. F. Allard, and D. C. Joy (Eds.), Kluwer, New York (1998) pp. 107–124.
28. D. C. Ghiglia and M. D. Pritt, *Two-Dimensional Phase Unwrapping: Theory, Algorithms and Software*, Wiley, New York (1998).
29. E. Völkl, L. F. Allard, and B. Frost, *Ultramicroscopy* 58 (1995) 97.
30. D. J. Smith and M. R. McCartney, In: *Introduction to Electron Holography*, E. Völkl, L. F. Allard, and D. C. Joy (Eds.), Kluwer, New York (1998) pp. 87–106.
31. M. R. McCartney, D. J. Smith, R. F. C. Farrow, and R. F. Marks, *J. Appl. Phys.* 82 (1997) 2461.
32. R. E. Dunin-Borkowski, M. R. McCartney, B. Kardynal, S. S. P. Parkin, M. R. Scheinfein, and D. J. Smith, *J. Microscopy* 200 (2000) 187.
33. S. M. Sze, *Physics of Semiconductor Devices*, Wiley, New York (2002).
34. S. Frabonni, G. Matteucci, G. Pozzi, and U. Valdre, *Phys. Rev. Lett*. 44 (1985) 2196.
35. M. R. McCartney, D. J. Smith, R. Hull, J. C. Bean, E. Völkl, and B. Frost, *Appl. Phys. Lett*. 65 (1994) 2603.
36. M. R. McCartney, M. A. Gribelyuk, J. Li, P. Ronsheim, J. S. McMurray, and D. J. Smith, *Appl. Phys. Lett*. 80 (2002) 3213.
37. M. A. Gribelyuk, M. R. McCartney, J. Li, C. S. Murthy, P. Ronsheim, B. Doris, J. S. McMurray, S. Hegde, and D. J. Smith, *Phys. Rev. Lett*. 89 (2002) 025502.
38. A. Twitchett, R. E. Dunin-Borkowski, and P. A. Midgley, *Phys. Rev. Lett*. 88 (2002) 238302.
39. A. Twitchett, R. E. Dunin-Borkowski, R. F. Broom, and P. A. Midgley, *J. Phys. Condens. Matt*. 16 (2004) S181.
40. W. D. Rau, P. Schwander, F. H. Baumann, W. Hoppner, and A. Ourmazd, *Phys. Rev. Lett* 82 (1999) 2614.
41. J. Li, M. R. McCartney, and D. J. Smith, *Ultramicroscopy* 94 (2003) 149.
42. H. Morkoç, *Nitride Semiconductors and Devices*, Springer, Berlin (1999).
43. J. Barnard and D. Cherns, *J. Electron Microscopy* 49 (2000) 281.
44. D. Cherns, H. Mokhtari, C. G. Jaio, R. Averback, and H. Riechert, *J. Cryst. Growth* 230 (2001) 410.
45. J. Cai and F. A. Ponce, *J. Appl. Phys.* 91 (2002) 9856.
46. J. Cai, F. A. Ponce, S. Tanaka, H. Omiya, and Y. Nakagawa, *phys. stat. sol.* (a) 188 (2001) 833.
47. M. R. McCartney, F. A. Ponce, J. Cai, and D. P. Bour, *Appl. Phys. Lett*. 76 (2000) 3055.
48. J. Cai and F. A. Ponce, *phys. stat. sol.* (a) 192 (2002) 407.
49. D. Cherns and C. G. Jiao, *Phys. Rev. Lett*. 87 (2001) 5504.
50. C. G. Jiao and D. Cherns, *J. Electron Microscopy* 51 (2002) 105.
51. I.-H. Tan, G. L. Snider, L. D. Chang, and E. L. Hu, *J. Appl. Phys.* 68 (1990) 4071.
52. A. Krtschil, A. Dadger, and A. Krosy, *Appl. Phys. Lett*. 82 (2003) 2263.

53. H.-J. Im, Y. Ding, J. P. Pelz, B. Heying, and J. S. Speck, *Phys. Rev. Lett*. 87 (2001) 106802.
54. R. Saito, G. Dresselhaus, and M. S. Dresselhaus, *Physical Properties of Carbon Nanotubes*, Imperial College Press, London (1999).
55. J. Cumings, A. Zettl, M. R. McCartney, and J. C. H. Spence, *Phys. Rev. Lett*. 88 (2002) 056804.
56. L. F. Allard, E. Völkl, D. S. Kalakkad, and A. K. Datye, J. *Mater. Sci*. 29 (1994) 5612.
57. L. F. Allard, E. Völkl, A. Carim, A. K. Datye, and R. Ruoff, *Nano. Mater*. 7 (1996) 137.
58. M. R. McCartney and M. Gajardziska-Josifovska, *Ultramicroscopy* 53 (1994) 283.
59. M. Gajdardziska-Josifovska and M. R. McCartney, *Ultramicroscopy* 53 (1994) 291.
60. J. K. Weiss, W. J. de Ruijter, M. Gajdardziska-Josifovska, M. R. McCartney, and D. J. Smith, *Ultramicroscopy* 50 (1993) 301.
61. M. Gajdardziska-Josifovska, *MSA Bulletin* 24 (1994) 507.
62. Y. Miura, *J. Magn. Magn. Mater*. 134 (1994) 209.
63. J. N. Chapman and M. R. Scheinfein, *J. Magn. Magn. Mater.* 200 (1999) 729.
64. R. E. Dunin-Borkowski, M. R. McCartney, B. Kardynal, and D. J. Smith, *J. Appl. Phys* 84 (1998) 374.
65. R. E. Dunin-Borkowski, M. R. McCartney, B. Kardynal, D. J. Smith, and M. R. Scheinfein, *Appl. Phys. Lett*. 75 (1999) 2641.
66. D. J. Smith, R. E. Dunin-Borkowski, M. R. McCartney, B. Kardynal, and M. R. Scheinfein, *J. Appl. Phys*. 87 (2000) 7400.
67. R. E. Dunin-Borkowski, M. R. McCartney, B. Kardynal, M. R. Scheinfein, D. J. Smith, and S. S. P. Parkin, *J. Appl. Phys.* 90 (2001) 2899.
68. S. S. P. Parkin, *Ann. Rev. Mater. Sci*. 25 (1995) 357.
69. D. A. Bazylinski and R. B. Frankel, In: *Biomineralization: From Biology to Biotechnology*, E. Bauerlein (Ed.), Wiley-VCH, Weinheim (2000).
70. R. E. Dunin-Borkowski, M. R. McCartney, R. B. Frankel, D. A. Bazylinski, M. Pósfai, and P. R. Buseck, *Science* 282 (1998) 1868.
71. R. E. Dunin-Borkowski, M. R. McCartney, M. Pösfai, R. B. Frankel, D. A. Bazylinski, and P. R. Buseck, *Eur. J. Mineral*. 13 (2001) 671.
72. M. R. McCartney, U. Lins, M. Farina, P. R. Buseck, and R. B. Frankel, *Eur. J. Mineral*. 13 (2001) 685.
73. M. J. Hÿtch, R. E. Dunin-Borkowski, J. Moulin, C. Duhamel, F. Mazaleyrat, and Y. Champion, *Phys. Rev. Lett*. 91 (2003) 257207.